

Fractional Quantum Hall Effect Based on Weyl Orbits

Jiong-Hao Wang¹, Yan-Bin Yang¹, and Yong Xu^{1,2*}

¹*Center for Quantum Information, IIS, Tsinghua University, Beijing 100084, People's Republic of China and*

²*Hefei National Laboratory, Hefei 230088, People's Republic of China*

The fractional quantum Hall effect is a well-known demonstration of strongly correlated topological phases in two dimensions. However, the extension of this phenomenon into a three-dimensional context has yet to be achieved. Recently, the three-dimensional integer quantum Hall effect based on Weyl orbits has been experimentally observed in a topological semimetallic material under a magnetic field. This motivates us to ask whether the Weyl orbits can give rise to the fractional quantum Hall effect when their Landau level is partially filled in the presence of interactions. Here we theoretically demonstrate that the fractional quantum Hall states based on Weyl orbits can emerge in a Weyl semimetal when a Landau level is one-third filled. Using concrete models for Weyl semimetals in magnetic fields, we project the Coulomb interaction onto a single Landau level from the Weyl orbit and find that the ground state of the many-body Hamiltonian is triply degenerate. We further show that the ground states exhibit the many-body Chern number of $1/3$ and the uniform occupation of electrons in both momentum and real space, implying that they are the fractional quantum Hall states. In contrast to the two-dimensional case, the states are spatially localized on two surfaces hosting Fermi arcs. Additionally, our findings suggest that the excitation properties of these states resemble those of the Laughlin state in two dimensions, as inferred from the particle entanglement spectrum of the ground states.

INTRODUCTION

The fractional quantum Hall (FQH) effect [1–5], originating from the interplay between topology and strong correlations, has been one of the central topics in condensed matter physics since its discovery [6]. The FQH states possess exotic properties including fractionally quantized Hall conductance [6, 7] as well as anyonic excitations with fractional charges [8–10]. They serve as a paradigmatic example of topological order [11–13] with long-range entanglement [14, 15] and have potential applications in topological quantum computation [16–18]. Although the study of FQH states has lasted for decades, it still awards us with new surprise, for example, the geometric degree of freedom [19] that gives rise to chiral gravitons [20–23]. Recently, the FQH effect has been realized in various quantum simulators with high controllability, including photons [24, 25] and cold atoms [26]. Its counterpart under no magnetic field, called fractional quantum anomalous Hall state or fractional Chern insulator [27–32], has been observed experimentally in moiré superlattice structures including twisted bilayer transition metal dichalcogenide material MoTe_2 [33–36] and rhombohedral pentalayer graphene-hBN heterostructure [37]. The progress provides new platforms for the study of the FQH states and gives chance to uncover more hidden treasure in this fascinating quantum matter. Despite the substantial advancements in experiments and theoretical understanding of the FQH states, the existing research focuses on two-dimensional (2D) systems, and the FQH physics in three dimensions (3D) is still elusive because the energy dispersion due to the additional dimension melts the separation of Landau levels, disfavoring the occurrence of the FQH

effect.

Weyl semimetals [38–42] host low-energy excitations with linear dispersions near the gapless Weyl points which come in pairs with positive and negative topological charges. The topological surface states named Fermi arcs connect Weyl points with opposite chirality and result in anomalous Hall conductivity [43, 44]. Remarkably, under the magnetic field, the Fermi arcs on opposite surfaces form the Weyl orbit [45] in the assistance of bulk Weyl points, leading to Landau levels supporting the 3D quantum Hall effect [46–60]. It is thus natural to ask whether the Weyl orbit can bring about the 3D FQH effect when the Landau level is partially filled with appropriate filling factor and the interaction is turned on. The answer is unclear because the Landau level emerging from the Weyl orbit is very different from the lowest Landau level in 2D (see Appendix B).

In this work, we theoretically demonstrate that the FQH effect based on Weyl orbits can arise in a Weyl semimetal under the magnetic field. By projecting the Coulomb interaction onto a Landau level originating from Weyl orbits, we obtain the energy spectrum of the many-body Hamiltonian using exact diagonalization for a one-third filled case. We find that the triply degenerate ground states occur in the specific total momentum sectors predicted by the generalized Pauli principle, which are identified as the FQH states justified by the many-body Chern number. The possibility of the charge density wave (CDW) is excluded because the fluctuation of the occupation number on each single-particle state is small and the real-space electron density is quite uniform in the plane parallel to the top and bottom surfaces, characteristic of a FQH fluid. The electron fluid concentrates on the top and bottom surfaces, which is a distinctive feature of the FQH effect based on Weyl

orbits, indicating its 3D nature. Despite the significant difference in the spatial character from the conventional FQH effect in a 2D electron gas, the excitation properties of the Weyl-orbit-based FQH states resemble those of the Laughlin state, manifesting in the particle entanglement spectrum. Finally, as real Weyl materials usually host multiple pairs of Weyl points, we study a time-reversal symmetric Weyl semimetal model with two pairs of Weyl points under a magnetic field and find that the FQH effect can also occur in this system based on Weyl orbits.

MODEL

To investigate the FQH effect based on Weyl orbits, we consider the following single-particle Hamiltonian of a Weyl semimetal in momentum space [46]

$$H(\mathbf{k}) = M[k_w^2 - (k_x^2 + k_y^2 + k_z^2)]\sigma_z + A(k_x\sigma_x + k_y\sigma_y) + [D_1k_y^2 + D_2(k_x^2 + k_z^2)]\sigma_0, \quad (1)$$

where $\mathbf{k} = (k_x, k_y, k_z)$ is the wave vector, σ_ν with $\nu = 0, x, y, z$ are identity and Pauli matrices, and k_w, M, A, D_1 and D_2 are real system parameters. The model hosts a pair of Weyl points at $\mathbf{k} = (0, 0, \pm k_w)$ in the bulk with the energy $E_W = D_2k_w^2$. Under open boundary conditions (OBCs) along y , the projections of the bulk Weyl points onto the top and bottom surfaces are connected by bent Fermi arcs as shown schematically in Fig. 1(a). The Fermi arcs lead to the Weyl orbit [a closed loop shown in Fig. 1(a)] in the presence of magnetic fields $\mathbf{B} = (0, B, 0)$ along y [45, 46, 52]. The Weyl orbit gives rise to Landau levels around the energy of the Weyl points, as shown in Fig. 1(b) (see Appendix A for the basis used to calculate the Landau levels). Here we set the parameters as $\tilde{M} = M/l_B^2 = 0.04E_0$, $\tilde{D}_1 = D_1/l_B^2 = 0.01E_0$, $\tilde{D}_2 = D_2/l_B^2 = 0.02E_0$, $\tilde{A} = A/l_B = 0.04E_0$ and $\tilde{k}_w = k_w l_B = 2.8$, where $l_B = \sqrt{\hbar/(eB)}$ is the magnetic length with \hbar being the reduced Planck constant and e being the elementary charge, and E_0 is the unit of energy. The above set of parameters are used throughout the paper.

To study the FQH effect, we include the following Coulomb interaction between electrons under periodic boundary conditions (PBCs) along x and z and OBCs along y ,

$$V(\mathbf{r}) = \sum_{t,s=-\infty}^{+\infty} \frac{e^2}{4\pi\epsilon} \frac{1}{\mathbf{r} + tL_x\mathbf{e}_x + sL_z\mathbf{e}_z}, \quad (2)$$

where t and s take integer values, ϵ is the dielectric constant, \mathbf{e}_x (\mathbf{e}_z) are the unit vectors along x (z), and L_x (L_z) is the length of the system along x (z). Since the sum of the Chern number of all the bands below the Landau level highlighted by the red line in Fig. 1(b) vanishes, we consider the case that this Landau level is one-third

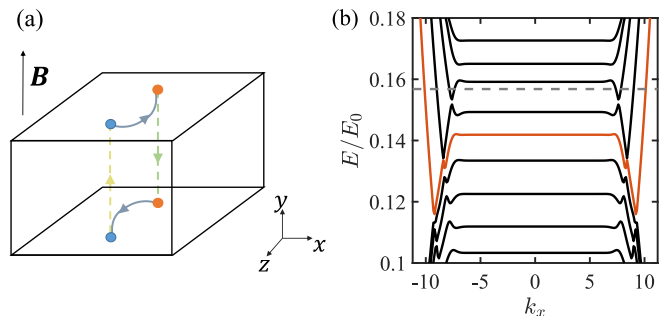


FIG. 1. (a) Schematic illustration of Fermi arcs and Weyl orbits formed under the magnetic field \mathbf{B} for the Hamiltonian (1). (b) The Landau levels of the Hamiltonian (1) near the energy of the Weyl points (the dashed grey line). The Landau level onto which the Coulomb interaction is projected is colored red. Here we take OBCs along y and PBCs along x . The system size used for the calculation is $\tilde{L}_y = L_y/(\sqrt{2\pi}l_B) = 4$ and $\tilde{L}_z = L_z/(\sqrt{2\pi}l_B) = 8$ with L_y and L_z the length of the system along y and z , respectively.

filled. Similar to the FQH effect in 2D or the fractional Chern insulator, in numerical calculations, we project the Coulomb interaction onto the Landau level and obtain the following many-body Hamiltonian

$$\hat{H}_I = \sum_{j_1, j_2, j_3, j_4=0}^{m_L-1} B_{j_1 j_2 j_3 j_4} \hat{a}_{j_1}^\dagger \hat{a}_{j_2}^\dagger \hat{a}_{j_3} \hat{a}_{j_4}, \quad (3)$$

where $\hat{a}_{j_\mu}^\dagger$ (\hat{a}_{j_μ}) is the creation (annihilation) operator corresponding to the single-particle state with momentum $k_x = 2\pi j_\mu/L_x$ in the considered Landau level. Here, the momentum quantum number j_μ with $\mu = 1, 2, 3, 4$ takes integer values from 0 to $m_L - 1$ where $m_L = L_x L_z / (2\pi l_B^2) = \tilde{L}_x \tilde{L}_z$ is the degeneracy of the Landau level with $\tilde{L}_x = L_x / (\sqrt{2\pi}l_B)$. The explicit form and detailed derivation of the coefficients $B_{j_1 j_2 j_3 j_4}$ can be found in Appendix C. The single-band projection method used here is commonly used in the study of the FQH effect and fractional Chern insulators, see, e.g., [28, 61, 62]. Note that we neglect the single-particle energy including the kinetic energy and the potential energy due to the interaction between an electron and its image under PBCs [61] in the Hamiltonian (3), because it only contributes a constant and does not alter the physics when the particle number is conserved.

MANY-BODY ENERGY SPECTRUM

To demonstrate the existence of the FQH effect based on Weyl orbits, we diagonalize the many-body Hamiltonian (3) for the electron number $n_e = 8, 10$ in a system with the degeneracy of the Landau level $m_L = 24, 30$, respectively. Since the Hamiltonian (3) is translationally invariant, K_x (the sum of the momentum quantum num-

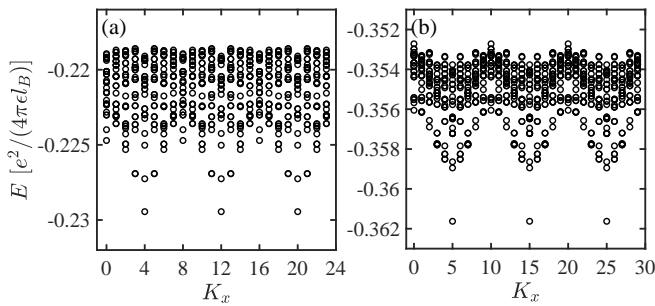


FIG. 2. The many-body energy spectrum with respect to the momentum quantum number K_x for (a) $n_e = 8$ and (b) $n_e = 10$. We take the aspect ratio $r_a = 1$ in (a) and $r_a = 0.8$ in (b).

ber j of all occupied single-particle states modulo m_L) is a good quantum number. In the calculations, we fix the thickness of the system to be $\tilde{L}_y = 4$ and take the aspect ratio $r_a = L_x/L_z$ to be $r_a = 1, 0.8$ for $n_e = 8, 10$, respectively.

Figure 2 displays the many-body energy spectrum with respect to K_x , illustrating the existence of the triply degenerate ground states for both the system sizes. The ground states occur at the momenta $K_x = 4, 12, 20$ for $n_e = 8$ and $K_x = 5, 15, 25$ for $n_e = 10$. The momenta are consistent with the theoretical prediction of the generalized Pauli principle for (1,3)-admissible partitions, that is, the maximum number of electrons in three consecutive orbitals is one [30, 63]. In addition, we observe the presence of an energy gap between the ground states and the first excited states. These results suggest that the ground states are the incompressible FQH states.

GROUND STATE PROPERTIES

To exclude the possibility of the CDW phase with the equal ground state degeneracy, we calculate the occupation numbers on all single-particle states labelled by the momentum quantum number j for each ground state, $n_j = \langle a_j^\dagger a_j \rangle$. As shown in Fig. 3(a), we see the occupation number on each single-particle state is always close to $1/3$ (indicated by the dashed grey line) for every ground state of the system with $n_e = 10$ electrons, consistent with the behavior of the FQH liquid. The slight deviations from the exact $1/3$ should be attributed to the finite-size effect [30].

In addition, we extract the electron number density $\rho(\mathbf{r})$ in real space and obtain the integrated density distribution $\rho_{xz}(x, z) = \int \rho(\mathbf{r}) dy$ in the (x, z) plane, exhibiting a quite uniform distribution with small fluctuations $\eta = (\max \rho_{xz} - \min \rho_{xz}) / \bar{\rho}_{xz} = 0.24\%$ where $\bar{\rho}_{xz}$ represents the average density (see Appendix D for the density distribution at a fixed y). The uniformity of the electron density in both momentum and real space

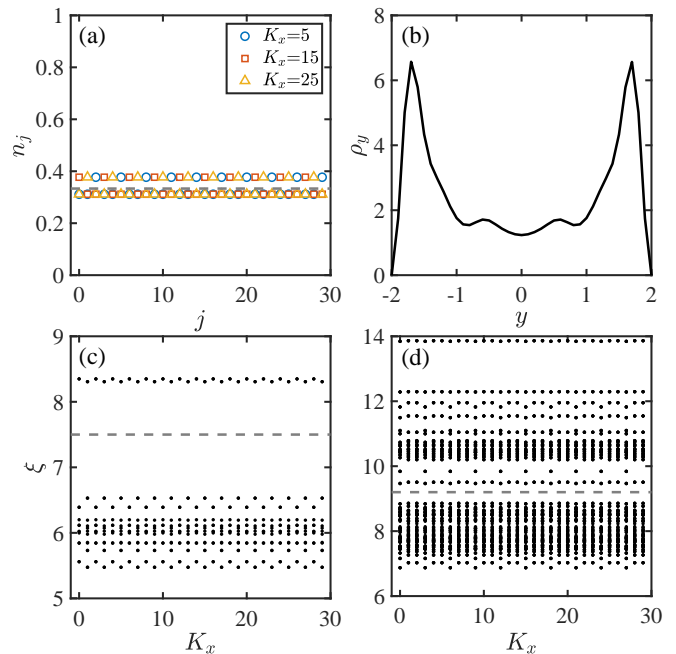


FIG. 3. (a) The occupation number on each single-particle state with the momentum quantum number j for the ground states with $K_x = 5$ (blue circle), 10 (red square) and 15 (yellow triangle) when $n_e = 10$. (b) The real-space electron density ρ_y of the ground state with $K_x = 5$ versus the y coordinate. The particle entanglement spectrum of the ground states for (c) $n_a = 2$ and (d) $n_a = 3$. The number of states below the gap (indicated by the dashed grey line) in each momentum sector is $12, 13, 12, 13, \dots, 12, 13$ in (c) and $85, 84, 84, 85, 84, 84, \dots, 85, 84, 84$ in (d), consistent with the (1,3) generalized Pauli principle.

evidence that the system is in the FQH phase rather than a CDW phase. To further investigate the spatial distribution of the electron liquid, we plot the integrated density distribution in the y direction $\rho_y(y) = \int \rho(\mathbf{r}) dx dz$ in Fig. 3(b). Clearly, we see that the electron fluid concentrates around the top and bottom surfaces where the Fermi arcs are located, in stark contrast to the conventional FQH effect in 2D. Note that the real-space electron density shown above is for the ground state with $K_x = 5$, and the results for the other two ground states are almost the same.

To diagnose the many-body topology of the ground states, we compute the Chern number by imposing the twisted boundary conditions along x, z [7, 28, 64] (also see Appendix E),

$$C = \frac{1}{2\pi} \int_0^{2\pi} d\theta_x \int_0^{2\pi} d\theta_z \text{Im} [\langle \partial_{\theta_x} \Psi | \partial_{\theta_z} \Psi \rangle - \text{c.c.}]. \quad (4)$$

Here $\Psi(\theta_x, \theta_z)$ is the wave function of the many-body ground state under boundary phases θ_x and θ_z , which transforms k_x to $k_x - \theta_x/L_x$ and k_z to $k_z - \theta_z/L_z$ in the Hamiltonian (1). For electron number $n_e = 8$, we find that the Chern numbers of the three ground states are

all 0.3321, very close to $1/3$, further confirming that the ground states are the FQH states.

To study the excitation properties of the FQH states arising from Weyl orbits, we calculate the particle entanglement spectrum [30, 65] (also see Appendix F), that is, the eigenvalues ξ of the reduced density matrix

$$\rho_A = \text{Tr}_B \left(\frac{1}{3} \sum_{i=1}^3 |\Psi_i\rangle\langle\Psi_i| \right), \quad (5)$$

where $|\Psi_i\rangle$ with $i = 1, 2, 3$ denote the three ground states. Here, we divide the n_e electrons into A and B part with n_a and n_b electrons, respectively. Tracing out the electrons in the B part corresponds to generating quasi-hole excitations [65]. For the total electron number $n_e = 10$, we show the particle entanglement spectrum for $n_a = 2$ and 3 with respect to the total momentum quantum number K_x in Fig. 3(c) and (d), based on the fact that ρ_A satisfies the conservation of momentum. We see a clear gap in the entanglement spectrum for both $n_a = 2$ and 3, indicated by the dashed grey line. For $n_a = 2$, the number of states below the gap is 12 when K_x is even and 13 when K_x is odd; for $n_a = 3$, the number is 85 when K_x is an integer multiple of 3 and 84 for other K_x . The number of states in each momentum sector coincides with the analytical results of the (1,3) generalized Pauli principle [30, 63], suggesting that the FQH states based on Weyl orbits with $\nu = 1/3$ share similar excitation properties to the Laughlin states for the 2D electron gas.

TIME-REVERSAL SYMMETRIC MODEL

For the generality of our results, we study a four-band model

$$\begin{aligned} H_T(\mathbf{k}) = & M[k_w^2 - (k_x^2 + k_y^2 + k_z^2)]s_0\sigma_z \\ & + A(k_x s_z \sigma_x + k_y s_0 \sigma_y) + \alpha k_y s_y \sigma_x \\ & + [D_1 k_y^2 + D_2(k_x^2 + k_z^2)]s_0\sigma_0 + \beta s_y \sigma_y \end{aligned} \quad (6)$$

with another set of identity and Pauli matrices s_0, s_x, s_y, s_z representing the spin degree of freedom. This model respects time-reversal symmetry, i.e. $TH_T(\mathbf{k})T^{-1} = H_T(-\mathbf{k})$ for the time-reversal operator $T = is_y\sigma_0\kappa$ with κ being the complex conjugate operator. The system has two pairs of Weyl points, and the projections of each pair onto the top and bottom surfaces are connected by Fermi arcs when we take OBCs along y , as shown schematically in Fig. 4(a). With a magnetic field $\mathbf{B} = (0, B, 0)$ along y , the Fermi arcs form two Weyl orbits assisted by the Weyl points [46, 60]. We plot the Landau levels near the energy of the Weyl points under PBCs along x and OBCs along y and z in Fig. 4(b). Here we include the Zeeman energy $H_Z = \Delta_Z s_y \sigma_0$ with $\Delta_Z = 0.006E_0$, $\tilde{\alpha} = \alpha/l_B = 0.08E_0$ and $\beta = 0.001E_0$ and other parameters the same as before.

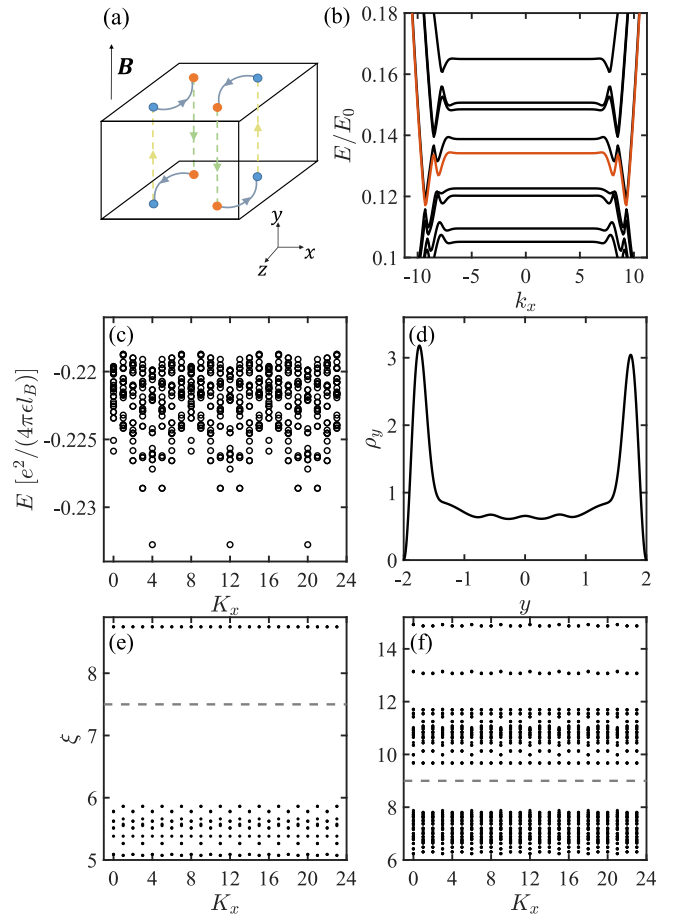


FIG. 4. (a) Schematic illustration of the time-reversal symmetric model (6) with two pairs of Weyl points, Fermi arcs and Weyl orbits formed under the magnetic field. (b) The Landau levels of the Hamiltonian (6) with the partially filled Landau level colored red. (c) The many-body energy spectrum of the interacting Hamiltonian, exhibiting the triply degenerate ground states. (d) The electron density distribution ρ_y along y of the ground state with $K_x = 4$. Note that the density distribution is the same for the other two ground states. The particle entanglement spectrum of the ground states for (e) $n_a = 2$ and (f) $n_a = 3$. In (c)-(f), $n_e = 8$.

To study the many-body physics when the Landau level we are interested in [colored red in Fig. 4(b)] are partially filled with $\nu = 1/3$, we project the Coulomb interaction (2) onto that Landau level under PBCs along x and z and OBCs along y . In Fig. 4(c), we plot the energy spectrum obtained by diagonalizing the projected many-body Hamiltonian for $n_e = 8$, illustrating the existence of triply degenerate ground states. Their positions in K_x are consistent with the prediction of the (1,3) generalized Pauli principle [30, 63]. In addition, by calculating the real-space electron density distribution $\rho(\mathbf{r})$ for a ground state, we find that the density distribution $\rho_{xz}(x, z)$ in the (x, z) plane is almost uniform with a tiny fluctuation $\eta = 0.48\%$, characteristic of a FQH liquid behavior.

Similar to the previous case, the electron liquid inhabits the top and bottom surfaces [see the electron density distribution ρ_y along y in Fig. 4(d)], which constitutes the distinctive character of the FQH effect based on the Weyl orbit. We further calculate the particle entanglement spectrum of the ground states for $n_a = 2$ and 3, as shown in Fig. 4(e) and (f). We see that under the gap indicated by the dashed grey line, the number of states is 9, 10, 9, 10, ..., 9, 10 in Fig. 4(e) and 46, 45, 45, 46, 45, 45, ..., 46, 45, 45 in Fig. 4(f), consistent with the generalized (1,3) Pauli principle. All these results suggest that the ground states are the FQH states.

In summary, we discover the FQH effect based on Weyl orbits in Weyl semimetals under a magnetic field. We identify the FQH effect by calculating the ground state degeneracy, the many-body Chern number, the density distribution and the entanglement spectrum. Unlike the 2D case, the FQH liquid is found to reside on two opposite surfaces of the 3D system. Given that the 3D integer quantum Hall effect has been experimentally observed in the topological semimetal Cd_3As_2 [47–50, 53], we expect that the FQH effect based on Weyl orbits may also be observed in this or other similar materials at lower temperatures. Our work opens a new direction for explor-

ing the FQH effect in 3D topological semimetals. Many interesting topics, such as composite Fermi liquid and non-Abelian FQH effect, merit further study.

We thank X. Gao for helpful discussions. This work is supported by the National Natural Science Foundation of China (Grant No. 12474265, 11974201) and Innovation Program for Quantum Science and Technology (Grant No. 2021ZD0301604). We also acknowledge the support by Center of High Performance Computing, Tsinghua University.

APPENDIX A: BASES USED TO DIAGONALIZE THE SINGLE-PARTICLE WEYL SEMIMETAL HAMILTONIAN UNDER A MAGNETIC FIELD

In this Appendix, we will show the basis chosen to diagonalize the Weyl semimetal Hamiltonian under the magnetic field in the main text for both open and periodic boundary conditions in the z direction.

We write the single-particle Weyl semimetal Hamiltonian (1) [46] in the main text in the following matrix form

$$H = \begin{pmatrix} (D_2 - M)(k_x^2 + k_z^2) + (D_1 - M)k_y^2 + Mk_w^2 & A(k_x - ik_y) \\ A(k_x + ik_y) & (D_2 + M)(k_x^2 + k_z^2) + (D_1 + M)k_y^2 - Mk_w^2 \end{pmatrix}. \quad (7)$$

For the magnetic field in the y direction $\mathbf{B} = (0, B, 0)$, we consider the Landau gauge by taking the vector potential $\mathbf{A} = (Bz, 0, 0)$. As a result, k_x is replaced by $k_x + z/l_B^2$ with the magnetic length $l_B = \sqrt{\hbar/eB}$, and k_z is replaced by $-i\partial_z$ due to the broken translational symmetry along

z . As the surface Fermi arc states are necessary to the Weyl orbit, we take open boundary conditions (OBCs) along y and replace k_y by $-i\partial_y$. We therefore arrive at the Hamiltonian under the magnetic field,

$$H_B = \begin{pmatrix} (D_2 - M)[(k_x + z/l_B^2)^2 - \partial_z^2] - (D_1 - M)\partial_y^2 + Mk_w^2 & A(k_x + z/l_B^2 - \partial_y) \\ A(k_x + z/l_B^2 + \partial_y) & (D_2 + M)[(k_x + z/l_B^2)^2 - \partial_z^2] - (D_1 + M)\partial_y^2 - Mk_w^2 \end{pmatrix} \quad (8)$$

with k_x being the only good quantum number.

For the calculation of Fig. 1(b) in the main text, we consider a system with a finite length L_z and OBCs in the z direction and choose the basis $|l, k\rangle$ with the real-space representation

$$\langle y, z | l, k \rangle = \frac{2}{\sqrt{L_y L_z}} \sin \left[\frac{l\pi}{L_y} \left(y + \frac{L_y}{2} \right) \right] \sin \left[\frac{k\pi}{L_z} \left(z + \frac{L_z}{2} \right) \right] \quad (9)$$

with $l, k = 1, 2, 3, \dots$ to diagonalize the Hamiltonian (8) such that the edge states appear in Fig. 1(b) where we take the cutoff $l, k \leq 60$.

If we focus on the bulk physics and do not want to see the edge states, we consider a system that is infinite in the z direction and choose the basis $|m, h\rangle = |m\rangle \otimes |h\rangle$ with $m = 0, 1, 2, \dots$ and $h = 1, 2, 3, \dots$ such that

$$\langle z | m \rangle = \frac{1}{\sqrt{\sqrt{\pi} 2^m m! l_B}} \exp \left[-\frac{(z - z_0)^2}{2l_B^2} \right] \mathcal{H}_m \left(\frac{z - z_0}{l_B} \right) \quad (10)$$

with the guiding center $z_0 = -k_x l_B^2$ and Hermite polynomials \mathcal{H}_m and

$$\langle y | h \rangle = \sqrt{\frac{2}{L_y}} \sin \left[\frac{h\pi}{L_y} \left(y + \frac{L_y}{2} \right) \right]. \quad (11)$$

$\langle z|m\rangle$ has the form of the wave function of the state in the m th Landau level in 2D and satisfies $\hat{b}^\dagger \hat{b}|m\rangle = m|m\rangle$, $\hat{b}^\dagger|m\rangle = \sqrt{m+1}|m+1\rangle$ and $\hat{b}|m\rangle = \sqrt{m}|m-1\rangle$ where

$$\hat{b}^\dagger = \frac{l_B}{\sqrt{2}} \left[k_x + \frac{z}{l_B^2} - i(-i\partial_z) \right], \quad (12)$$

$$H_B = \left(\begin{array}{c} \frac{2(D_2-M)}{l_B^2} (\hat{b}^\dagger \hat{b} + \frac{1}{2}) - (D_1 - M)\partial_y^2 + Mk_w^2 \\ A[\frac{\hat{b}^\dagger + \hat{b}}{\sqrt{2}l_B} + \partial_y] \end{array} \quad \begin{array}{c} A[\frac{\hat{b}^\dagger + \hat{b}}{\sqrt{2}l_B} - \partial_y] \\ \frac{2(D_2+M)}{l_B^2} (\hat{b}^\dagger \hat{b} + \frac{1}{2}) - (D_1 + M)\partial_y^2 - Mk_w^2 \end{array} \right). \quad (14)$$

By diagonalizing the Hamiltonian (14) under the basis $|m, h\rangle$, we get the u th eigenstate

$$|u\rangle = \sum_{m,h,\sigma} c_{m,h,\sigma}^u |m, h\rangle \otimes |\sigma\rangle. \quad (15)$$

with $\sigma = 0, 1$ representing the pseudospin degree of freedom and the real-space wave function is the spinor

$$\mathbf{f}^u = (f_0^u, f_1^u)^T \quad (16)$$

with $f_\sigma^u(y, z) = \langle y, z, \sigma | u \rangle$. Note that the diagonalization process is performed in the subspace with a specific momentum k_x , so the complete real-space wave function of the corresponding eigenstate is $\tilde{\phi}^u = (\tilde{\phi}_0^u, \tilde{\phi}_1^u)^T$ where

$$\begin{aligned} \tilde{\phi}_\sigma^u(x, y, z) &= e^{ik_x x} f_\sigma^u(y, z) \\ &= \sum_{m,h} c_{m,h,\sigma}^u \tilde{\psi}_{m,h}(x, y, z) \end{aligned} \quad (17)$$

with

$$\begin{aligned} \tilde{\psi}_{m,h}(x, y, z) &= \sqrt{\frac{2}{\sqrt{\pi} 2^m m! l_B L_y}} \exp \left[ik_x x - \frac{(z - z_0)^2}{2l_B^2} \right] \\ &\quad \mathcal{H}_m \left(\frac{z - z_0}{l_B} \right) \sin \left[\frac{h\pi}{L_y} \left(y + \frac{L_y}{2} \right) \right]. \end{aligned} \quad (18)$$

In the main text, when we project the Coulomb interaction onto a Landau level, we consider the system with the finite length L_x, L_z and periodic boundary conditions (PBCs) in the x, z directions. In this case, the eigenstate wave function is $(\phi_{0,j}^u, \phi_{1,j}^u)^T$ where

$$\phi_{\sigma,j}^u(x, y, z) = \sum_{m,h} c_{m,h,\sigma}^u \psi_{m,h,j}(x, y, z) \quad (19)$$

with

$$\begin{aligned} \psi_{m,h,j}(x, y, z) &= \sqrt{\frac{2}{\sqrt{\pi} 2^m m! l_B L_y}} \\ &\quad \sum_{n=-\infty}^{+\infty} \exp \left[i \left(\frac{2\pi j}{L_x} + \frac{nL_z}{l_B^2} \right) x - \frac{(z - z_n)^2}{2l_B^2} \right] \\ &\quad \mathcal{H}_m \left(\frac{z - z_n}{l_B} \right) \sin \left[\frac{h\pi}{L_y} \left(y + \frac{L_y}{2} \right) \right]. \end{aligned} \quad (20)$$

$$\hat{b} = \frac{l_B}{\sqrt{2}} \left[k_x + \frac{z}{l_B^2} + i(-i\partial_z) \right]. \quad (13)$$

In terms of \hat{b}^\dagger and \hat{b} , the Hamiltonian (8) is expressed as

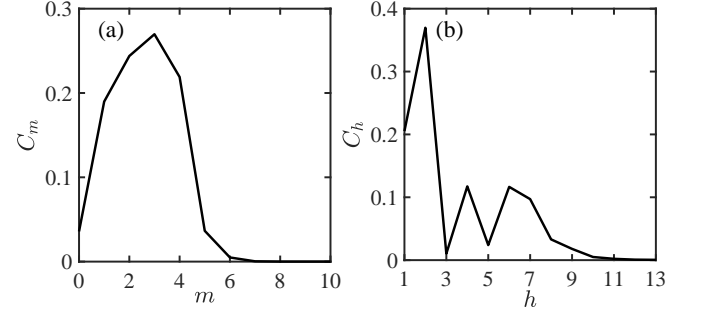


FIG. 5. The probability (a) C_m and (b) C_h for a state in the considered Landau level in the main text [colored red in Fig. 1(b)].

Here, $z_n = -2\pi j l_B^2 / L_x - nL_z$ where the momentum quantum number $j = 0, 1, 2, \dots, m_L - 1$ with $m_L = L_x L_z / (2\pi l_B^2)$ being the Landau level degeneracy. The basis wave function satisfies $\psi_{m,h,j}(x, y, z + L_z) = e^{-iL_z x / l_B^2} \psi_{m,h,j}(x, y, z)$ and $\psi_{m,h,j}(x + L_x, y, z) = \psi_{m,h,j}(x, y, z)$, which is consistent with the magnetic translation operator $\mathcal{T}_{\mathbf{R}}$ acting as $\mathcal{T}_{\mathbf{R}}\psi(\mathbf{r}) = e^{i\mathbf{x}R_z / l_B^2} \psi(\mathbf{r} + \mathbf{R})$ under the gauge vector $\mathbf{A} = (Bz, 0, 0)$ with $\mathbf{R} = (R_x, 0, R_z)$ being the translation vector.

APPENDIX B: PROPERTIES OF THE LANDAU LEVEL BASED ON WEYL ORBITS

In this Appendix, we will show the weight of the considered Landau level based on Weyl orbits in the wave functions in the considered basis so as to validate the cutoff used for the calculation in the main text and provide the real-space wave function to illustrate that the Landau level based on Weyl orbits is very different from the lowest Landau level in 2D.

We first show the probability that an eigenstate in the considered Landau level in the main text is found at different m and h ,

$$C_m = \sum_{h,\sigma} |c_{m,h,\sigma}^u|^2, \quad (21)$$

and

$$C_h = \sum_{m,\sigma} |c_{m,h,\sigma}^u|^2. \quad (22)$$

In Fig. 5(a), we see that the maximum value of C_m locates at $m = 3$ and the value at $m = 0$ is relatively small compared with that at $m = 1, 2, 3, 4$. For larger m , C_m quickly drops to 0, so we take the cutoff $m \leq 8$ for the calculation of the interacting Hamiltonian (3) in the main text. With the increasing of h , C_h reaches the maximum at $h = 2$ and then undergoes a sharp drop, followed by an oscillation before decaying to 0, as shown in Fig. 5(b). We thus take the cutoff $h \leq 13$ in the main text. To justify the validity of the cutoff, we also calculate the many-body spectrum with larger m and h and find that the spectrum almost does not change up to $m = 13$ and $h = 20$, revealing that the above cutoff used in the main text is enough.

To show that the Landau level based on Weyl orbits is very different from the lowest Landau level in 2D, we plot the wave function \mathbf{f}^u in Eq. (16) versus z at certain y for a system with thickness $L_y = 4$ and $y \in [-L_y/2, L_y/2]$ in Fig. 6. Around the surface, as shown in Fig. 6(a) for $y = -1.7$, the component f_0^u exhibits two nodes if we neglect the tiny dip near $z = \pm 1$. Going inside into the bulk, f_0^u hosts four nodes at $y = -1.1$ [see Fig. 6(b)] and three nodes at $y = 0$ [see Fig. 6(c)]. For the other component f_1^u , the numbers of nodes are 2, 3, 4 at $y = -1.7, -1.1, 0$, as shown in Fig. 6(d),(e) and (f). We thus see that the Landau level based on Weyl orbits is distinct from the lowest Landau level in 2D which carries no nodes. It is therefore not immediately apparent that the FQH effect can also occur in this system.

APPENDIX C: THE COEFFICIENTS OF THE INTERACTING HAMILTONIAN

In this Appendix, we will derive the coefficients $B_{j_1 j_2 j_3 j_4}$ of the interacting Hamiltonian (3) in the main text in detail. The interacting Hamiltonian in the second quantization form reads

$$\hat{H}_I = \frac{1}{2} \int d\mathbf{r}_1 \int d\mathbf{r}_2 \sum_{\sigma_1, \sigma_2} \Psi_{\sigma_1}^\dagger(\mathbf{r}_1) \Psi_{\sigma_2}^\dagger(\mathbf{r}_2) V(\mathbf{r}_1 - \mathbf{r}_2) \Psi_{\sigma_2}(\mathbf{r}_2) \Psi_{\sigma_1}(\mathbf{r}_1), \quad (23)$$

where $\Psi_\sigma^\dagger(\mathbf{r})$ and $\Psi_\sigma(\mathbf{r})$ are creation and annihilation field operators with the pseudospin degree of freedom σ ,

$$V(\mathbf{r}) = \sum_{t,s=-\infty}^{+\infty} \frac{e^2}{4\pi\epsilon} \frac{1}{\mathbf{r} + tL_x \mathbf{e}_x + sL_z \mathbf{e}_z} \quad (24)$$

is the Coulomb interaction under PBCs in the x and z directions, and $\int d\mathbf{r} := \int_0^{L_x} dx \int_{-L_y/2}^{L_y/2} dy \int_{-L_z}^0 dz$ for a

system with the length L_x, L_y, L_z in the x, y, z directions, respectively. Under the approximation of the single band projection,

$$\Psi_\sigma^\dagger(\mathbf{r}) = \sum_{j=0}^{m_L-1} \phi_{\sigma,j}^{*u}(\mathbf{r}) a_j^\dagger \quad (25)$$

and

$$\Psi_\sigma(\mathbf{r}) = \sum_{j=0}^{m_L-1} \phi_{\sigma,j}^u(\mathbf{r}) a_j \quad (26)$$

where $\phi_{\sigma,j}^u$ is the wave function of the state with the momentum quantum number j in the Landau level that we project the Coulomb interaction onto and $\hat{a}_{j\mu}^\dagger$ ($\hat{a}_{j\mu}$) is the corresponding creation (annihilation) operator. Substituting Eq. (25) and Eq. (26) into Eq. (23) and using Eq. (19), we get

$$\hat{H}_I = \sum_{j_1 j_2 j_3 j_4} \frac{1}{2} \int d\mathbf{r}_1 \int d\mathbf{r}_2 \sum_{\sigma_1, \sigma_2} \phi_{\sigma_1, j_1}^{*u}(\mathbf{r}_1) \phi_{\sigma_2, j_2}^{*u}(\mathbf{r}_2) V(\mathbf{r}_1 - \mathbf{r}_2) \phi_{\sigma_2, j_3}^u(\mathbf{r}_2) \phi_{\sigma_1, j_4}^u(\mathbf{r}_1) \hat{a}_{j_1}^\dagger \hat{a}_{j_2}^\dagger \hat{a}_{j_3} \hat{a}_{j_4}, \quad (27)$$

so the coefficient in Eq. (3) in the main text is

$$B_{j_1 j_2 j_3 j_4} = \frac{1}{2} \int d\mathbf{r}_1 \int d\mathbf{r}_2 \sum_{\sigma_1, \sigma_2} \phi_{\sigma_1, j_1}^{*u}(\mathbf{r}_1) \phi_{\sigma_2, j_2}^{*u}(\mathbf{r}_2) V(\mathbf{r}_1 - \mathbf{r}_2) \phi_{\sigma_2, j_3}^u(\mathbf{r}_2) \phi_{\sigma_1, j_4}^u(\mathbf{r}_1) = \sum_{\sigma_1 \sigma_2} \sum_{m_1, 2, 3, 4} c_{m_1, h_1, \sigma_1}^{*u} c_{m_2, h_2, \sigma_2}^{*u} c_{m_3, h_3, \sigma_2}^u c_{m_4, h_4, \sigma_1}^u A_{j_1 j_2 j_3 j_4}^{m_1 h_1 m_2 h_2 m_3 h_3 m_4 h_4} \quad (28)$$

where

$$A_{j_1 j_2 j_3 j_4}^{m_1 h_1 m_2 h_2 m_3 h_3 m_4 h_4} = \frac{1}{2} \int d\mathbf{r}_1 \int d\mathbf{r}_2 \psi_{m_1 h_1 j_1}^*(\mathbf{r}_1) \psi_{m_2 h_2 j_2}^*(\mathbf{r}_2) V(\mathbf{r}_1 - \mathbf{r}_2) \psi_{m_3 h_3 j_3}(\mathbf{r}_2) \psi_{m_4 h_4 j_4}(\mathbf{r}_1). \quad (29)$$

To evaluate $A_{j_1 j_2 j_3 j_4}^{m_1 h_1 m_2 h_2 m_3 h_3 m_4 h_4}$, we make use of the explicit form of $\psi_{m,h,j}(\mathbf{r})$ in Eq. (20) and the Fourier transform in the x and z directions of the Coulomb interaction

$$V(q_x, q_z, y) = \frac{1}{L_x L_z} \frac{2\pi e^{-q|y|}}{q}, \quad (30)$$

where $q = \sqrt{q_x^2 + q_z^2}$ such that

$$V(\mathbf{r}) = \sum'_{q_x, q_z, s, t} V(\mathbf{q}, y) e^{iq_x x + iq_z z} \delta_{q_x, \frac{2\pi}{L_x} t} \delta_{q_z, \frac{2\pi}{L_z} s} \quad (31)$$

with $\mathbf{q} = (q_x, q_z)$ and s, t taking integer values from $-\infty$ to $+\infty$ excluding 0, indicated by the symbol $'$ on the summation symbol. We can safely drop the coefficient with $\mathbf{q} = \mathbf{0}$ because it becomes a constant proportional to the electron density, which will be cancelled by the

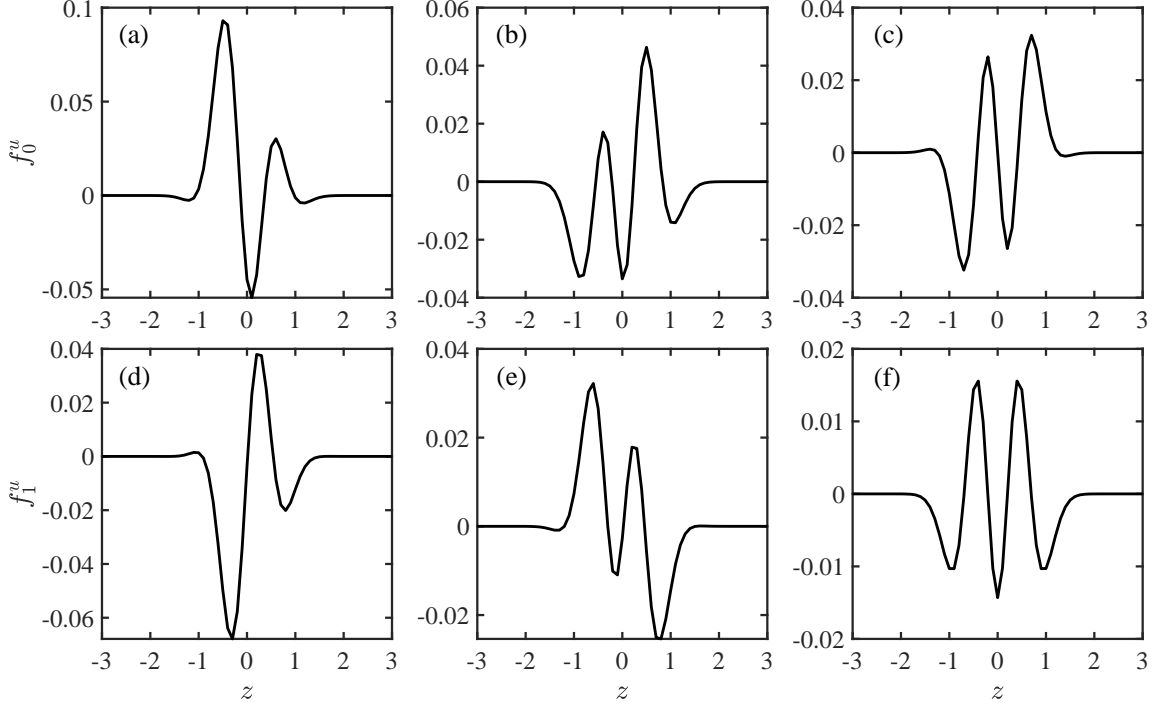


FIG. 6. The wave function versus z [the f_0^u (f_1^u) component in the first (second) row] of the considered Landau level state based on Weyl orbits at a fixed y . In (a) and (d), $y = -1.7$, in (b) and (e), $y = -1.1$, and in (c) and (f), $y = 0$.

positive charge background in the thermodynamic limit. In a finite system, it only contributes a constant to the diagonal elements of the many-body Hamiltonian and does not change the physics, see, e.g. the Supplemental Material in Ref. [66]. Then

$$A_{j_1 j_2 j_3 j_4}^{m_1 h_1 m_2 h_2 m_3 h_3 m_4 h_4} = \frac{1}{2L_x L_z} \sum'_{q_x, q_z, s, t} \frac{2\pi}{q} F(\mathbf{q}) S_1(\mathbf{q}) S_2(\mathbf{q}) \delta_{q_x, \frac{2\pi}{L_x} t} \delta_{q_z, \frac{2\pi}{L_z} s}, \quad (32)$$

where

$$F(\mathbf{q}) = \int_{-L_y/2}^{L_y/2} \int_{-L_y/2}^{L_y/2} dy_1 dy_2 \left(\frac{2}{L_y}\right)^2 \sin\left[\frac{h_1 \pi}{L_y} \left(y_1 + \frac{L_y}{2}\right)\right] \sin\left[\frac{h_4 \pi}{L_y} \left(y_1 + \frac{L_y}{2}\right)\right] \sin\left[\frac{h_2 \pi}{L_y} \left(y_2 + \frac{L_y}{2}\right)\right] \sin\left[\frac{h_3 \pi}{L_y} \left(y_2 + \frac{L_y}{2}\right)\right] e^{-q|y_1 - y_2|}, \quad (33)$$

$$S_1(\mathbf{q}) = a \sum_{n_1 n_4} \int_0^{L_x} dx_1 \frac{1}{L_x} e^{-i \left[\frac{2\pi}{L_x} (j_1 - j_4) + \frac{(n_1 - n_4) L_z}{l_B^2} - q_x \right] x_1} \int_{-L_z}^0 dz_1 e^{iq_z z_1} e^{-[(Z_{j_1} + n_1 L_z + z_1)^2 + (Z_{j_4} + n_4 L_z + z_1)^2]/(2l_B^2)} H_{m_1}[(z_1 + Z_{j_1} + n_1 L_z)/l_B] H_{m_4}[(z_1 + Z_{j_4} + n_4 L_z)/l_B], \quad (34)$$

$$S_2(\mathbf{q}) = a \sum_{n_2 n_3} \int_0^{L_x} dx_2 \frac{1}{L_x} e^{-i \left[\frac{2\pi}{L_x} (j_2 - j_3) + \frac{(n_2 - n_3) L_z}{l_B^2} + q_x \right] x_2} \int_{-L_z}^0 dz_2 e^{iq_z z_2} e^{-[(Z_{j_2} + n_2 L_z + z_2)^2 + (Z_{j_3} + n_3 L_z + z_2)^2]/(2l_B^2)} H_{m_2}[(z_2 + Z_{j_2} + n_2 L_z)/l_B] H_{m_3}[(z_2 + Z_{j_3} + n_3 L_z)/l_B] \quad (35)$$

with $Z_j = 2\pi j l_B^2 / L_x$, $a = 1/(l_B \sqrt{\pi} \sqrt{2^{m_1 + m_4} m_1! m_4!})$. In the following, we derive $S_1(\mathbf{q})$, and some explanations for certain steps can be found after Eq. (42).

$$S_1(\mathbf{q}) = a \sum_{\Delta n} \delta_{q_x, \frac{2\pi}{L_x} [j_1 - j_4 + \Delta n m_L]} \int_{-L_z}^0 \sum_n dz_1 e^{iq_z z_1} e^{-[(Z_{j_1} + \Delta n L_z + z_1 + n L_z)^2 + (Z_{j_4} + z_1 + n L_z)^2]/(2l_B^2)} H_{m_1}[(z_1 + n L_z + Z_{j_1} + \Delta n L_z)/l_B] H_{m_4}[(z_1 + n L_z + Z_{j_4})/l_B] \quad (36)$$

$$= a \sum_{\Delta n} \delta_{q_x, \frac{2\pi}{L_x} [j_1 - j_4 + \Delta n m_L]} \int_{-\infty}^{+\infty} dz_1 e^{iq_z z_1} e^{-[(Z_{j_1} + \Delta n L_z + z_1)^2 + (Z_{j_4} + z_1)^2]/(2l_B^2)} H_{m_1}[(z_1 + Z_{j_1} + \Delta n L_z)/l_B] H_{m_4}[(z_1 + Z_{j_4})/l_B] \quad (37)$$

$$= a \sum_{\Delta n} \delta_{q_x, \frac{2\pi}{L_x}[j_1-j_4+\Delta n m_L]} \lim_{t_1, t_4 \rightarrow 0} \frac{d^{m_1}}{dt_1^{m_1}} \frac{d^{m_4}}{dt_4^{m_4}} \int_{-\infty}^{+\infty} dz_1 e^{iq_z z_1} e^{-[(Z_{j_1}+\Delta n L_z+z_1)^2+(Z_{j_4}+z_1)^2]/(2l_B^2)} e^{-t_1^2+2t_1(z_1+Z_{j_1}+\Delta n L_z)/l_B-t_4^2+2t_4(z_1+Z_{j_4})/l_B} \quad (38)$$

$$= a \sum_{\Delta n} \delta_{q_x, \frac{2\pi}{L_x}[j_1-j_4+\Delta n m_L]} \lim_{t_1, t_4 \rightarrow 0} \frac{d^{m_1}}{dt_1^{m_1}} \frac{d^{m_4}}{dt_4^{m_4}} e^{-\frac{[(Z_{j_1}+\Delta n L_z)^2+Z_{j_4}^2]}{2l_B^2}+2\frac{Z_{j_1}+\Delta n L_z}{l_B}t_1+2\frac{Z_{j_4}}{l_B}t_4-t_1^2-t_4^2} \int_{-\infty}^{+\infty} dz_1 e^{iq_z z_1} e^{[-z_1^2-(Z_{j_1}+\Delta n L_z+Z_{j_4}-2t_1 l_B-2t_4 l_B)x_1]/l_B^2} \quad (39)$$

$$= a' \sum_{\Delta n} \delta_{q_x, \frac{2\pi}{L_x}[j_1-j_4+\Delta n m_L]} \lim_{t_1, t_4 \rightarrow 0} \frac{d^{m_1}}{dt_1^{m_1}} \frac{d^{m_4}}{dt_4^{m_4}} e^{-\frac{[(Z_{j_1}+\Delta n L_z)^2+Z_{j_4}^2]}{2l_B^2}+2\frac{Z_{j_1}+\Delta n L_z}{l_B}t_1+2\frac{Z_{j_4}}{l_B}t_4-t_1^2-t_4^2+\gamma^2/l_B^2-q_z^2 l_B^2/4+iq_z \gamma} \quad (40)$$

$$= a' \sum_{\Delta n} \delta_{q_x, \frac{2\pi}{L_x}[j_1-j_4+\Delta n m_L]} e^{-q_z^2 l_B^2/4-[(Z_{j_1}+\Delta n L_z)-Z_{j_4}]^2/(4l_B^2)-iq_z(Z_{j_1}+\Delta n L_z+Z_{j_4})/2} \lim_{t_1, t_4 \rightarrow 0} \frac{d^{m_1}}{dt_1^{m_1}} \frac{d^{m_4}}{dt_4^{m_4}} e^{[(Z_{j_1}+\Delta n L_z)-Z_{j_4}]t_1/l_B-[(Z_{j_1}+\Delta n L_z)-Z_{j_4}]t_4/l_B+2t_1 t_4+i(t_1+t_4)q_z l_B} \quad (41)$$

$$= a' \sum_{\Delta n} \delta_{q_x, \frac{2\pi}{L_x}[j_1-j_4+\Delta n m_L]} e^{-q^2 l_B^2/4-iq_z(Z_{j_1}+\Delta n L_z+Z_{j_4})/2} \lim_{t_1, t_4 \rightarrow 0} \frac{d^{m_1}}{dt_1^{m_1}} \frac{d^{m_4}}{dt_4^{m_4}} e^{q_x l_B(t_1-t_4)+2t_1 t_4+i(t_1+t_4)q_z l_B}. \quad (42)$$

From Eq. (34) to Eq. (36), we use $n = n_4$, $\Delta n = n_1 - n_4$ and $m_L = L_x L_z / (2\pi l_B^2)$. From Eq. (36) to Eq. (37), we utilize the Poisson summation rule. We use the generating function of the Hermite polynomial

$$\frac{d^m}{dt^m} e^{-t^2+2tx} = H_m(x) \quad (43)$$

to derive from Eq. (37) to Eq. (38). From Eq. (39) to Eq. (40), we use the complex form Gaussian integral

$$\int_{-\infty}^{+\infty} dx e^{iq_x x} e^{-x^2+sx} = \sqrt{\pi} e^{(s^2-q^2)/4+iqs/2} \quad (44)$$

and $a' = a l_B \sqrt{\pi} = 1/(2^{m_1+m_4} m_1! m_4!)$ as well as $\gamma = -(Z_{j_1} + \Delta n L_z + Z_{j_4} - 2t_1 l_B - 2t_4 l_B)/2$. We use $[Z_{j_1} + \Delta n L_z - Z_{j_4}]/l_B^2 = q_x$ due to $\delta_{q_x, 2\pi[j_1-j_4+\Delta n m_L]/L_x}$ to arrive at Eq. (42).

When $m_1 \leq m_4$,

$$S_1(\mathbf{q}) = \frac{1}{\sqrt{2^{m_1+m_4} m_1! m_4!}} \sum_{\Delta n} \delta_{q_x, \frac{2\pi}{L_x}[j_1-j_4+\Delta n m_L]} e^{-q^2 l_B^2/4-iq_z(Z_{j_1}+\Delta n L_z+Z_{j_4})/2} \lim_{t_1, t_4 \rightarrow 0} \frac{d^{m_1}}{dt_1^{m_1}} \frac{d^{m_4}}{dt_4^{m_4}} e^{(2t_1-q_x l_B+iq_z l_B)t_4+(q_x l_B+iq_z l_B)t_1} \quad (45)$$

$$= \frac{2^{m_4}}{\sqrt{2^{m_1+m_4} m_1! m_4!}} \sum_{\Delta n} \delta_{q_x, \frac{2\pi}{L_x}[j_1-j_4+\Delta n m_L]} e^{-q^2 l_B^2/4-iq_z(Z_{j_1}+\Delta n L_z+Z_{j_4})/2} \lim_{t_1 \rightarrow 0} \frac{d^{m_1}}{dt_1^{m_1}} (t_1 - q_x l_B/2 + iq_z l_B/2)^{m_4} e^{(q_x l_B+iq_z l_B)t_1} \quad (46)$$

$$= \frac{2^{m_4}}{\sqrt{2^{m_1+m_4} m_1! m_4!}} \sum_{\Delta n} \delta_{q_x, \frac{2\pi}{L_x}[j_1-j_4+\Delta n m_L]} e^{-q^2 l_B^2/4-iq_z(Z_{j_1}+\Delta n L_z+Z_{j_4})/2} \sum_{u=0}^{m_1} [(q_x + iq_z)l_B]^{m_1-u} \left[\frac{(-q_x + iq_z)l_B}{2} \right]^{m_4-u} \frac{m_4!}{(m_4-u)!} \frac{m_1!}{(m_1-u)!} u! \quad (47)$$

$$= \sqrt{\frac{m_1!}{m_4!}} 2^K \sum_{\Delta n} \delta_{q_x, \frac{2\pi}{L_x}[j_1-j_4+\Delta n m_L]} e^{-q^2 l_B^2/4-iq_z(Z_{j_1}+\Delta n L_z+Z_{j_4})/2}$$

$$\left[\frac{(-q_x + iq_z)l_B}{2}\right]^K \sum_{s=0}^{m_1} (-1)^s \left(\frac{q^2 l_B^2}{2}\right)^s \frac{m_4!}{(s+K)!s!(m_1-s)!} \quad (48)$$

$$= \sqrt{\frac{m_1!}{m_4!}} \sum_{\Delta n} \delta_{q_x, \frac{2\pi}{L_x}[j_1-j_4+\Delta n m_L]} e^{-q^2 l_B^2/4 - iq_z(Z_{j_1}+\Delta n L_z+Z_{j_4})/2} \left[\frac{(-q_x + iq_z)l_B}{\sqrt{2}}\right]^K \mathcal{L}_{m_1}^{(K)}\left(\frac{q^2 l_B^2}{2}\right). \quad (49)$$

From Eq. (46) to Eq. (47), we use the formula

$$\frac{d^n}{dx^n} [(x-\alpha)^m e^{-\beta x}] = e^{-\beta x} \sum_{i=0}^n (-\beta)^{n-i} \frac{m!}{(m-i)!} \frac{n!}{(n-i)!} (x-\alpha)^{m-i}, \quad n \leq m \quad (50)$$

which can be proved by the mathematical induction. From Eq. (47) to Eq. (48), $m_1 - m_4$ is substituted by K and $m_4 - u$ is substituted by s . In Eq. (49), the associated Laguerre polynomial $\mathcal{L}_{m_1}^{(K)}$ can be expressed in the Rodrigues representation

$$L_n^{(k)}(x) = \sum_{s=0}^n \frac{(-1)^s (n+k)! x^s}{(n-s)!(s+k)!s!}. \quad (51)$$

When $m_1 > m_4$, the derivation is similar except that the derivative with respect to m_1 is evaluated earlier than that with respect to m_4 . We arrive at

$$S_1(\mathbf{q}) = \sqrt{\frac{m_4!}{m_1!}} \sum_{\Delta n} \delta_{q_x, \frac{2\pi}{L_x}[j_1-j_4+\Delta n m_L]}$$

$$e^{-q^2 l_B^2/4 - iq_z(Z_{j_1}+\Delta n L_z+Z_{j_4})/2} \left[\frac{(q_x + iq_z)l_B}{\sqrt{2}}\right]^K \mathcal{L}_{m_1}^{(K)}\left(\frac{q^2 l_B^2}{2}\right). \quad (52)$$

Combining Eq. (49) and Eq. (52), we get

$$S_1(\mathbf{q}) = \sqrt{\frac{\min(m_1, m_4)!}{\max(m_1, m_4)!}} \sum_{\Delta n} \delta_{q_x, \frac{2\pi}{L_x}[j_1-j_4+\Delta n m_L]} e^{-q^2 l_B^2/4 - iq_z(Z_{j_1}+\Delta n L_z+Z_{j_4})/2} \left[\frac{\text{sgn}(m_1 - m_4)q_x + iq_z}{\sqrt{2}} l_B\right]^{|m_1-m_4|} L_{\min(m_1, m_4)}^{(|m_1-m_4|)}\left(\frac{q^2 l_B^2}{2}\right). \quad (53)$$

In the same way, we obtain

$$S_2(\mathbf{q}) = \sqrt{\frac{\min(m_2, m_3)!}{\max(m_2, m_3)!}} \sum_{\Delta n'} \delta_{q_x, \frac{2\pi}{L_x}[j_3-j_2+\Delta n' m_L]} e^{-q^2 l_B^2/4 + iq_z(Z_{j_2}+\Delta n' L_z+Z_{j_3})/2} \left[\frac{-\text{sgn}(m_2 - m_3)q_x - iq_z}{\sqrt{2}} l_B\right]^{|m_2-m_3|} L_{\min(m_2, m_3)}^{(|m_2-m_3|)}\left(\frac{q^2 l_B^2}{2}\right). \quad (54)$$

Combining Eq. (53) and Eq. (54), we have

$$S_1(\mathbf{q})S_2(\mathbf{q})\delta_{q_x, \frac{2\pi}{L_x}t}\delta_{q_z, \frac{2\pi}{L_z}s} = G_1(\mathbf{q})G_2(\mathbf{q}) \sum_{\Delta n \Delta n'} \delta_{q_x, \frac{2\pi}{L_x}[j_1-j_4+\Delta n m_L]} \delta_{q_x, \frac{2\pi}{L_x}[j_3-j_2+\Delta n' m_L]} e^{iq_z(Z_{j_2}+Z_{j_3}-Z_{j_1}-Z_{j_4}+\Delta n' L_z+\Delta n L_z)/2} \quad (55)$$

$$= G_1(\mathbf{q})G_2(\mathbf{q}) \sum_{\Delta n \Delta n'} \delta_{t, j_1-j_4+\Delta n m_L} \delta_{j_1-j_4+\Delta n m_L, j_3-j_2+\Delta n' m_L} e^{i\frac{\pi s(j_2+j_3-j_1-j_4)}{m_L} + is\pi(\Delta n + \Delta n')} \quad (56)$$

$$= G_1(\mathbf{q})G_2(\mathbf{q}) \sum_{\Delta n \Delta n'} \delta_{t, j_1-j_4+\Delta n m_L} \delta_{j_2-j_4, j_3-j_1+(\Delta n' - \Delta n)m_L} e^{i\frac{2\pi s(j_3-j_1)}{m_L} + is\pi(\Delta n + \Delta n' + \Delta n' - \Delta n)} \quad (57)$$

$$= G_1(\mathbf{q})G_2(\mathbf{q})\delta'_{t, j_1-j_4} \delta'_{j_1+j_2, j_3+j_4} e^{i\frac{2\pi s(j_3-j_1)}{m_L}}, \quad (58)$$

where the prime on the δ function represents that the

equality is defined module m_L and

$$G_1(\mathbf{q}) = \sqrt{\frac{\min(m_1, m_4)!}{\max(m_1, m_4)!}} e^{-q^2 l_B^2/4}$$

$$\left[\frac{\text{sgn}(m_1 - m_4)q_x + iq_z}{\sqrt{2}} l_B \right]^{|m_1 - m_4|} L_{\min(m_1, m_4)}^{(|m_1 - m_4|)} \left(\frac{q^2 l_B^2}{2} \right), \quad (59)$$

$$\left[\frac{-\text{sgn}(m_2 - m_3)q_x - iq_z}{\sqrt{2}} l_B \right]^{|m_2 - m_3|} L_{\min(m_2, m_3)}^{(|m_2 - m_3|)} \left(\frac{q^2 l_B^2}{2} \right). \quad (60)$$

$$G_2(\mathbf{q}) = \sqrt{\frac{\min(m_2, m_3)!}{\max(m_2, m_3)!}} e^{-q^2 l_B^2 / 4}$$

In summary,

$$A_{j_1 j_2 j_3 j_4}^{m_1 h_1 m_2 h_2 m_3 h_3 m_4 h_4} = \frac{1}{2L_x L_z} \sum_{q_x, q_z, s, t} \frac{2\pi}{q} F(\mathbf{q}) G_1(\mathbf{q}) G_2(\mathbf{q}) e^{i \frac{2\pi s(j_3 - j_1)}{m_L}} \delta_{q_x, \frac{2\pi}{L_x} t} \delta_{q_z, \frac{2\pi}{L_z} s} \delta'_{t, j_1 - j_4} \delta'_{j_1 + j_2, j_3 + j_4}. \quad (61)$$

APPENDIX D: THE REAL-SPACE DENSITY DISTRIBUTION AT A FIXED y

In the main text, we show that the real-space density distribution of the calculated FQH liquid averaged over y is nearly uniform in the (x, z) plane. In this Appendix, we will provide the density distribution at any fixed y to illustrate its near uniformity.

We calculate the fluctuation of the real-space density distribution in the (x, z) plane at a fixed value of y ,

$$\gamma(y) = \frac{\rho_{\max}(y) - \rho_{\min}(y)}{\bar{\rho}(y)}, \quad (62)$$

where $\rho_{\max}(y)$, $\rho_{\min}(y)$ and $\bar{\rho}(y)$ represent the maximum, minimum and average value of the density $\rho(\mathbf{r})$ over the (x, z) plane at a specific y , respectively. The result is shown in Fig. 7 where we see that the fluctuation is small, within 9% at the maximum point for $n_e = 8$ electrons and within 8% for $n_e = 10$ electrons. The fluctuation for $n_e = 10$ is smaller than that for $n_e = 8$, suggesting that the finite fluctuation is due to the finite-size effect. In addition, we plot the density in the (x, z) plane near the bottom and top surfaces for $n_e = 10$ electrons in Fig. 7(b) and (c) and find that the density distributions exhibit a slight stripe pattern. Note that the single-particle states in our calculations are also localized along z and extended along x due to our gauge choice, supporting that the stripe pattern in the density distribution of the many-body ground state is attributed to our basis choice for the finite-size system.

APPENDIX E: THE MANY-BODY CHERN NUMBER

In the main text, we calculate the many-body Chern number by imposing twisted boundary phases $\boldsymbol{\theta} = (\theta_x, \theta_z)$ [7], which transforms k_x to $k_x - \theta_x/L_x$ and k_z to $k_z - \theta_z/L_z$ in the single-particle Hamiltonian (8). In

terms of \hat{b}^\dagger and \hat{b} in Eq. (12) and Eq. (13), we obtain

$$H_B = \begin{pmatrix} H_{11} & A[\frac{\hat{b}^\dagger + \hat{b}}{\sqrt{2}l_B} - \partial_y - \frac{\theta_x}{L_x}] \\ A[\frac{\hat{b}^\dagger + \hat{b}}{\sqrt{2}l_B} + \partial_y - \frac{\theta_x}{L_x}] & H_{22} \end{pmatrix}. \quad (63)$$

where

$$\begin{aligned} H_{11} = & \frac{2(D_2 - M)}{l_B^2} [\hat{b}^\dagger \hat{b} + \frac{1}{2} - \frac{l_B \theta_x}{\sqrt{2}L_x} (\hat{b} + \hat{b}^\dagger) \\ & + i \frac{l_B \theta_z}{\sqrt{2}L_z} (\hat{b} - \hat{b}^\dagger) + (\frac{\theta_x}{L_x})^2 + (\frac{\theta_z}{L_z})^2] \\ & - (D_1 - M) \partial_y^2 + M k_w^2, \end{aligned} \quad (64)$$

$$\begin{aligned} H_{22} = & \frac{2(D_2 + M)}{l_B^2} [\hat{b}^\dagger \hat{b} + \frac{1}{2} - \frac{l_B \theta_x}{\sqrt{2}L_x} (\hat{b} + \hat{b}^\dagger) \\ & + i \frac{l_B \theta_z}{\sqrt{2}L_z} (\hat{b} - \hat{b}^\dagger) + (\frac{\theta_x}{L_x})^2 + (\frac{\theta_z}{L_z})^2] \\ & - (D_1 + M) \partial_y^2 - M k_w^2. \end{aligned} \quad (65)$$

The single-particle eigenstate wave function is $[\phi_{0,j}^u(\boldsymbol{\theta}), \phi_{1,j}^u(\boldsymbol{\theta})]^T$ where

$$\phi_{\sigma,j}^u(x, y, z, \boldsymbol{\theta}) = \sum_{m,h} c_{m,h,\sigma}^u(\boldsymbol{\theta}) \psi_{m,h,j}(x, y, z) \quad (66)$$

with the basis $\psi_{m,h,j}(x, y, z)$ the same as (20). By projecting the Coulomb interaction onto one Landau level under the boundary phase $\boldsymbol{\theta}$ and diagonalizing the many-body Hamiltonian, we have the many-body ground state

$$|\Psi_M(\boldsymbol{\theta})\rangle = \sum_{\{j\}} O_{\{j\}}(\boldsymbol{\theta}) \{\hat{a}_j^\dagger(\boldsymbol{\theta})\} |0\rangle, \quad (67)$$

where $\{\hat{a}_j^\dagger(\boldsymbol{\theta})\} = \hat{a}_{j_1}^\dagger(\boldsymbol{\theta}) \hat{a}_{j_2}^\dagger(\boldsymbol{\theta}) \dots \hat{a}_{j_{n_e}}^\dagger(\boldsymbol{\theta})$ is a sequence of creation operators creating the Fock basis with $\hat{a}_j^\dagger(\boldsymbol{\theta})$ corresponding to the single-particle state $\phi_{\sigma,j}^u(x, y, z, \boldsymbol{\theta})$ on the specific Landau level under the boundary phase $\boldsymbol{\theta}$. $O_{\{j\}}(\boldsymbol{\theta})$ is the coefficient for each Fock basis with $\{j\} = j_1 j_2 \dots j_{n_e}$ and n_e being the number of electrons.

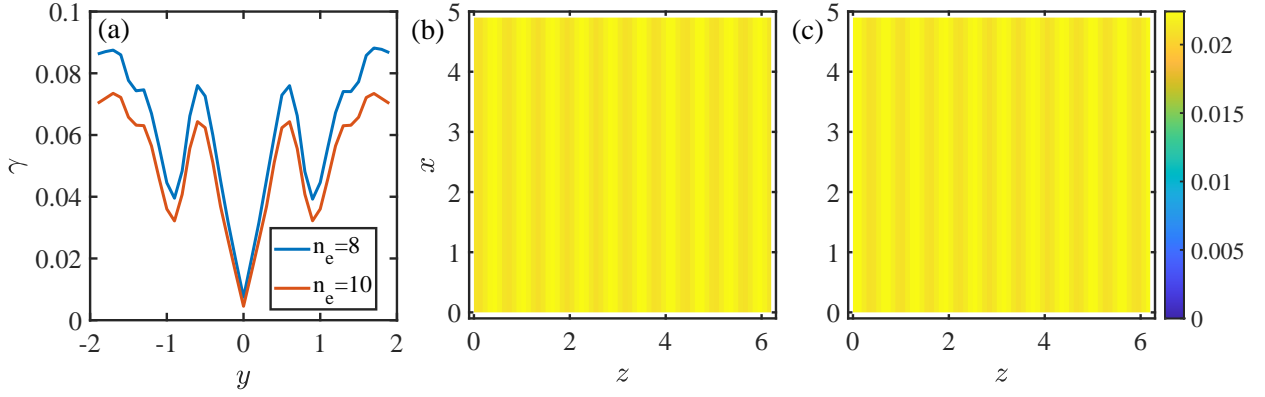


FIG. 7. (a) The fluctuation of the real-space density for 8 (blue line) and 10 (red line) electrons. Here we show the result of the ground state with $K_x = 20$ for $n_e = 8$ and $K_x = 25$ for $n_e = 10$, and the results of the other ground states are the same. The real-space density distribution in the (x, z) plane at (b) $y = -1.7$ and (c) $y = 1.7$ for the ground state with $K_x = 25$ for $n_e = 10$. The aspect ratio is $r_a = 1$ for $n_e = 8$ and $r_a = 0.8$ for $n_e = 10$, at which the gap between the triply degenerate ground states and excited states is maximum.

To evaluate the many-body Chern number, we use the method proposed in [64] for the discrete Brillouin zone:

$$C = \frac{1}{2\pi i} \sum_{\theta_0} \ln \left[\langle \Psi_M(\theta_0) | \Psi_M(\theta_0 + \hat{\theta}_x) \rangle \right. \\ \left. \langle \Psi_M(\theta_0 + \hat{\theta}_x) | \Psi_M(\theta_0 + \hat{\theta}_x + \hat{\theta}_y) \rangle \right. \\ \left. \langle \Psi_M(\theta_0 + \hat{\theta}_x + \hat{\theta}_y) | \Psi_M(\theta_0 + \hat{\theta}_y) \rangle \right. \\ \left. \langle \Psi_M(\theta_0 + \hat{\theta}_y) | \Psi_M(\theta_0) \rangle \right] \quad (68)$$

where $\hat{\theta}_x = (2\pi/N_x, 0)$, $\hat{\theta}_z = (0, 2\pi/N_z)$ with N_x, N_z taking integer values and $\theta_0 = (2\pi s/N_x, 2\pi t/N_z)$ with $s = 0, 1, 2, \dots, N_x - 1$ and $t = 0, 1, 2, \dots, N_z - 1$. Using Eq. (66) and Eq. (67), we get

$$\langle \Psi_M(\theta_1) | \Psi_M(\theta_2) \rangle = \sum_{\{j\}} O_{\{j\}}^*(\theta_1) O_{\{j\}}(\theta_2) \\ \left[\sum_{m,h,\sigma} c_{m,h,\sigma}^{*u}(\theta_1) c_{m,h,\sigma}^u(\theta_2) \right]^{n_e}. \quad (69)$$

For the calculation in the main text, we take $N_x = N_z = 20$.

APPENDIX F: THE PARTICLE-ENTANGLEMENT SPECTRUM

In this Appendix, we will review the method for calculating the particle-entanglement spectrum [30, 65] in detail, especially on how to decompose the Fock basis to partition the electrons into two parts.

To calculate the particle-entanglement spectrum of a many-body state $|\Psi\rangle$ with N orbitals and n_e electrons, we divide the n_e electrons into A and B part with n_a and n_b electrons, respectively, where $n_a + n_b = n_e$. Tracing

out the electrons in part B , we obtain the reduced density matrix

$$\rho_A = \text{Tr}_B(|\Psi\rangle\langle\Psi|), \quad (70)$$

the eigenvalues of which are just the entanglement spectrum. Taking the partial trace in terms of two parts of particles is not as straightforward as two blocks of orbitals. The key point is to decompose each Fock basis with N orbitals and n_e electrons into the tensor product of two other Fock basis, both with N orbitals while one with n_a electrons and another with n_b electrons. We will explain in detail in the following.

We use a sequence $\{j\} = [j_1 j_2 \dots j_{n_e}]$ to represent a Fock basis with N orbitals and n_e electrons, for which the j_i th orbital is occupied and we place the j_i in an ascending order. Obviously, $j_i \in \{1, 2, \dots, N\}$ and all the j_i in the same sequence are different from each other. For example, for $N = 6$ and $n_e = 3$, the sequence $\{j\} = [256]$ represents the Fock basis $|010011\rangle$. For the purpose of dividing the electrons into two parts, $\{j\}$ is decomposed as

$$\{j\} = \frac{1}{\sqrt{N_p}} \sum_{\{k\}} (-1)^t \{k\} \{l\}, \quad (71)$$

where $\{k\}$ and $\{l\}$ are also sequences representing Fock basis with $\{k\} = [k_1 k_2 \dots k_{n_a}]$, $\{l\} = [l_1 l_2 \dots l_{n_b}]$ and $k_i, l_i \in \{1, 2, \dots, N\}$, and $N_p = \binom{n_e}{n_a}$ denotes the number of the divided parts. The combination of $\{k\}$ and the corresponding $\{l\}$, i.e. $\{k\} \cup \{l\} = [k_1 k_2 \dots k_{n_a} l_1 l_2 \dots l_{n_b}]$ must recover $\{j\}$ up to a permutation. If an odd permutation is needed to recover $\{j\}$, t is odd and otherwise, t is even. Let us explain the method by an explicit example. If we decompose the basis $\{j\} = [256]$ with $N = 6$ orbitals into two parts with $n_a = 1$ and $n_b = 2$ electrons,

respectively,

$$[256] = \frac{1}{\sqrt{3}}([2][56] - [5][26] + [6][25]), \quad (72)$$

representing

$$\begin{aligned} |010011\rangle = & \frac{1}{\sqrt{3}}(|010000\rangle|000011\rangle - |000010\rangle|010001\rangle \\ & + |000001\rangle|010010\rangle). \end{aligned} \quad (73)$$

It is easy to check the equality in Eq. (73) by writing both sides in the form of first-quantized wave functions. As the many-body state $|\Psi\rangle$ is a superposition of the Fock basis with N orbitals and n_e electrons, it can be written in the form $|\Psi\rangle = \sum_{\{j\}\{k\}} c_{\{j\}}(-1)^t\{k\}\{l\}$ where $c_{\{j\}}$ is the coefficient before the basis $\{j\}$ after normalization. By tracing out the B part with n_b electrons, i.e. the $\{l\}$, we get the reduced density matrix ρ_A and then the particle-entanglement spectrum by the exact diagonalization.

* yongxuphy@tsinghua.edu.cn

- [1] J. Jain, Microscopic theory of the fractional quantum hall effect, *Adv. Phys.* **41**, 105 (1992).
- [2] H. L. Stormer, D. C. Tsui, and A. C. Gossard, The fractional quantum hall effect, *Rev. Mod. Phys.* **71**, S298 (1999).
- [3] H. L. Stormer, Nobel lecture: The fractional quantum hall effect, *Rev. Mod. Phys.* **71**, 875 (1999).
- [4] G. Murthy and R. Shankar, Hamiltonian theories of the fractional quantum hall effect, *Rev. Mod. Phys.* **75**, 1101 (2003).
- [5] T. H. Hansson, M. Hermanns, S. H. Simon, and S. F. Viefers, Quantum hall physics: Hierarchies and conformal field theory techniques, *Rev. Mod. Phys.* **89**, 025005 (2017).
- [6] D. C. Tsui, H. L. Stormer, and A. C. Gossard, Two-dimensional magnetotransport in the extreme quantum limit, *Phys. Rev. Lett.* **48**, 1559 (1982).
- [7] Q. Niu, D. J. Thouless, and Y.-S. Wu, Quantized hall conductance as a topological invariant, *Phys. Rev. B* **31**, 3372 (1985).
- [8] R. B. Laughlin, Anomalous quantum hall effect: An incompressible quantum fluid with fractionally charged excitations, *Phys. Rev. Lett.* **50**, 1395 (1983).
- [9] D. Arovas, J. R. Schrieffer, and F. Wilczek, Fractional statistics and the quantum hall effect, *Phys. Rev. Lett.* **53**, 722 (1984).
- [10] B. I. Halperin, Statistics of quasiparticles and the hierarchy of fractional quantized hall states, *Phys. Rev. Lett.* **52**, 1583 (1984).
- [11] X. G. Wen and Q. Niu, Ground-state degeneracy of the fractional quantum hall states in the presence of a random potential and on high-genus riemann surfaces, *Phys. Rev. B* **41**, 9377 (1990).
- [12] X.-G. Wen, Topological orders and edge excitations in fractional quantum hall states, *Adv. Phys.* **44**, 405 (1995).
- [13] X.-G. Wen, Colloquium: Zoo of quantum-topological phases of matter, *Rev. Mod. Phys.* **89**, 041004 (2017).
- [14] A. Kitaev and J. Preskill, Topological entanglement entropy, *Phys. Rev. Lett.* **96**, 110404 (2006).
- [15] M. Levin and X.-G. Wen, Detecting topological order in a ground state wave function, *Phys. Rev. Lett.* **96**, 110405 (2006).
- [16] G. Moore and N. Read, Nonabelions in the fractional quantum hall effect, *Nucl. Phys. B* **360**, 362 (1991).
- [17] N. Read and E. Rezayi, Beyond paired quantum hall states: Parafermions and incompressible states in the first excited landau level, *Phys. Rev. B* **59**, 8084 (1999).
- [18] C. Nayak, S. H. Simon, A. Stern, M. Freedman, and S. Das Sarma, Non-abelian anyons and topological quantum computation, *Rev. Mod. Phys.* **80**, 1083 (2008).
- [19] F. D. M. Haldane, Geometrical description of the fractional quantum hall effect, *Phys. Rev. Lett.* **107**, 116801 (2011).
- [20] B. Yang, Z.-X. Hu, Z. Papić, and F. D. M. Haldane, Model wave functions for the collective modes and the magnetoroton theory of the fractional quantum hall effect, *Phys. Rev. Lett.* **108**, 256807 (2012).
- [21] S. Golkar, D. X. Nguyen, and D. T. Son, Spectral sum rules and magneto-roton as emergent graviton in fractional quantum hall effect, *J. High Energy Phys.* **2016**, 21.
- [22] S.-F. Liou, F. D. M. Haldane, K. Yang, and E. H. Rezayi, Chiral gravitons in fractional quantum hall liquids, *Phys. Rev. Lett.* **123**, 146801 (2019).
- [23] J. Liang, Z. Liu, Z. Yang, Y. Huang, U. Wurstbauer, C. R. Dean, K. W. West, L. N. Pfeiffer, L. Du, and A. Pinczuk, Evidence for chiral graviton modes in fractional quantum hall liquids, *Nature* **628**, 78 (2024).
- [24] L. W. Clark, N. Schine, C. Baum, N. Jia, and J. Simon, Observation of Laughlin states made of light, *Nature* **582**, 41 (2020).
- [25] C. Wang, F.-M. Liu, M.-C. Chen, H. Chen, X.-H. Zhao, C. Ying, Z.-X. Shang, J.-W. Wang, Y.-H. Huo, C.-Z. Peng, X. Zhu, C.-Y. Lu, and J.-W. Pan, Realization of fractional quantum hall state with interacting photons, *Science* **384**, 579 (2024).
- [26] J. Léonard, S. Kim, J. Kwan, P. Segura, F. Grusdt, C. Repellin, N. Goldman, and M. Greiner, Realization of a fractional quantum hall state with ultracold atoms, *Nature* **619**, 495 (2023).
- [27] T. Neupert, L. Santos, C. Chamon, and C. Mudry, Fractional quantum hall states at zero magnetic field, *Phys. Rev. Lett.* **106**, 236804 (2011).
- [28] D. N. Sheng, Z.-C. Gu, K. Sun, and L. Sheng, Fractional quantum hall effect in the absence of Landau levels, *Nat. Commun.* **2**, 389 (2011).
- [29] Y.-F. Wang, Z.-C. Gu, C.-D. Gong, and D. N. Sheng, Fractional quantum hall effect of hard-core bosons in topological flat bands, *Phys. Rev. Lett.* **107**, 146803 (2011).
- [30] N. Regnault and B. A. Bernevig, Fractional Chern insulator, *Phys. Rev. X* **1**, 021014 (2011).
- [31] E. Tang, J.-W. Mei, and X.-G. Wen, High-temperature fractional quantum hall states, *Phys. Rev. Lett.* **106**, 236802 (2011).
- [32] K. Sun, Z. Gu, H. Katsura, and S. Das Sarma, Nearly flatbands with nontrivial topology, *Phys. Rev. Lett.* **106**, 236803 (2011).
- [33] J. Cai, E. Anderson, C. Wang, X. Zhang, X. Liu, W. Holtzmann, Y. Zhang, F. Fan, T. Taniguchi, K. Watanabe, Y. Ran, T. Cao, L. Fu, D. Xiao, W. Yao,

- and X. Xu, Signatures of fractional quantum anomalous hall states in twisted mote2, *Nature* **622**, 63 (2023).
- [34] Y. Zeng, Z. Xia, K. Kang, J. Zhu, P. Knüppel, C. Vaswani, K. Watanabe, T. Taniguchi, K. F. Mak, and J. Shan, Thermodynamic evidence of fractional chern insulator in moiré mote2, *Nature* **622**, 69 (2023).
- [35] H. Park, J. Cai, E. Anderson, Y. Zhang, J. Zhu, X. Liu, C. Wang, W. Holtzmann, C. Hu, Z. Liu, T. Taniguchi, K. Watanabe, J.-H. Chu, T. Cao, L. Fu, W. Yao, C.-Z. Chang, D. Cobden, D. Xiao, and X. Xu, Observation of fractionally quantized anomalous hall effect, *Nature* **622**, 74 (2023).
- [36] F. Xu, Z. Sun, T. Jia, C. Liu, C. Xu, C. Li, Y. Gu, K. Watanabe, T. Taniguchi, B. Tong, J. Jia, Z. Shi, S. Jiang, Y. Zhang, X. Liu, and T. Li, Observation of integer and fractional quantum anomalous hall effects in twisted bilayer $\{\mathrm{MoTe}\}_2$, *Phys. Rev. X* **13**, 031037 (2023).
- [37] Z. Lu, T. Han, Y. Yao, A. P. Reddy, J. Yang, J. Seo, K. Watanabe, T. Taniguchi, L. Fu, and L. Ju, Fractional quantum anomalous hall effect in multilayer graphene, *Nature* **626**, 759 (2024).
- [38] S. Jia, S.-Y. Xu, and M. Z. Hasan, Weyl semimetals, fermi arcs and chiral anomalies, *Nat. Mater.* **15**, 1140 (2016).
- [39] A. A. Burkov, Topological semimetals, *Nat. Mater.* **15**, 1145 (2016).
- [40] N. P. Armitage, E. J. Mele, and A. Vishwanath, Weyl and dirac semimetals in three-dimensional solids, *Rev. Mod. Phys.* **90**, 015001 (2018).
- [41] Y. Xu, Topological gapless matters in three-dimensional ultracold atomic gases, *Front. Phys.* **14**, 43402 (2019).
- [42] B. Q. Lv, T. Qian, and H. Ding, Experimental perspective on three-dimensional topological semimetals, *Rev. Mod. Phys.* **93**, 025002 (2021).
- [43] K.-Y. Yang, Y.-M. Lu, and Y. Ran, Quantum hall effects in a weyl semimetal: Possible application in pyrochlore iridates, *Phys. Rev. B* **84**, 075129 (2011).
- [44] A. A. Burkov and L. Balents, Weyl semimetal in a topological insulator multilayer, *Phys. Rev. Lett.* **107**, 127205 (2011).
- [45] A. C. Potter, I. Kimchi, and A. Vishwanath, Quantum oscillations from surface fermi arcs in weyl and dirac semimetals, *Nat. Commun.* **5**, 5161 (2014).
- [46] C. M. Wang, H.-P. Sun, H.-Z. Lu, and X. C. Xie, 3D quantum hall effect of fermi arcs in topological semimetals, *Phys. Rev. Lett.* **119**, 136806 (2017).
- [47] C. Zhang, A. Narayan, S. Lu, J. Zhang, H. Zhang, Z. Ni, X. Yuan, Y. Liu, J.-H. Park, E. Zhang, W. Wang, S. Liu, L. Cheng, L. Pi, Z. Sheng, S. Sanvito, and F. Xiu, Evolution of weyl orbit and quantum hall effect in dirac semimetal cd3as2, *Nat. Commun.* **8**, 1272 (2017).
- [48] M. Uchida, Y. Nakazawa, S. Nishihaya, K. Akiba, M. Kriener, Y. Kozuka, A. Miyake, Y. Taguchi, M. Tokunaga, N. Nagaosa, Y. Tokura, and M. Kawasaki, Quantum hall states observed in thin films of dirac semimetal cd3as2, *Nat. Commun.* **8**, 2274 (2017).
- [49] T. Schumann, L. Galletti, D. A. Kealhofer, H. Kim, M. Goyal, and S. Stemmer, Observation of the quantum hall effect in confined films of the three-dimensional dirac semimetal $\{\mathrm{Cd}\}_3\{\mathrm{As}\}_2$, *Phys. Rev. Lett.* **120**, 016801 (2018).
- [50] C. Zhang, Y. Zhang, X. Yuan, S. Lu, J. Zhang, A. Narayan, Y. Liu, H. Zhang, Z. Ni, R. Liu, E. S. Choi, A. Suslov, S. Sanvito, L. Pi, H.-Z. Lu, A. C. Potter, and F. Xiu, Quantum hall effect based on weyl orbits in cd3as2, *Nature* **565**, 331 (2019).
- [51] H.-Z. Lu, 3d quantum hall effect, *Nat. Sci. Rev.* **6**, 208 (2019).
- [52] H. Li, H. Liu, H. Jiang, and X. C. Xie, 3d quantum hall effect and a global picture of edge states in weyl semimetals, *Phys. Rev. Lett.* **125**, 036602 (2020).
- [53] S. Nishihaya, M. Uchida, Y. Nakazawa, M. Kriener, Y. Taguchi, and M. Kawasaki, Intrinsic coupling between spatially-separated surface fermi-arcs in weyl orbit quantum hall states, *Nat. Commun.* **12**, 2572 (2021).
- [54] R. Chen, T. Liu, C. M. Wang, H.-Z. Lu, and X. C. Xie, Field-tunable one-sided higher-order topological hinge states in dirac semimetals, *Phys. Rev. Lett.* **127**, 066801 (2021).
- [55] C. Zhang, Y. Zhang, H.-Z. Lu, X. C. Xie, and F. Xiu, Cycling fermi arc electrons with weyl orbits, *Nat. Rev. Phys.* **3**, 660 (2021).
- [56] S. Li, C. M. Wang, Z. Z. Du, F. Qin, H.-Z. Lu, and X. C. Xie, 3d quantum hall effects and nonlinear hall effect, *npj Quantum Mater.* **6**, 1 (2021).
- [57] M. Chang, Y. Ge, and L. Sheng, Generalization of the theory of three-dimensional quantum hall effect of fermi arcs in weyl semimetal, *Chin. Phys. B* **31**, 057304 (2022).
- [58] F. Xiong, C. Honerkamp, D. M. Kennes, and T. Nag, Understanding the three-dimensional quantum hall effect in generic multi-weyl semimetals, *Phys. Rev. B* **106**, 045424 (2022).
- [59] X. Zhang, Y. Lee, V. Kakani, K. Yang, K. Cho, and X. Shi, Two types of three-dimensional quantum hall effects in multilayer WTe₂, *Phys. Rev. B* **107**, 245410 (2023).
- [60] J.-H. Wang and Y. Xu, Three-dimensional quantum hall effect in topological amorphous metals (2023), arXiv:2309.05990 [cond-mat].
- [61] D. Yoshioka, B. I. Halperin, and P. A. Lee, Ground state of two-dimensional electrons in strong magnetic fields and 1/3 quantized hall effect, *Phys. Rev. Lett.* **50**, 1219 (1983).
- [62] C. Wang, X.-W. Zhang, X. Liu, Y. He, X. Xu, Y. Ran, T. Cao, and D. Xiao, Fractional chern insulator in twisted bilayer $\{\mathrm{MoTe}\}_2$, *Phys. Rev. Lett.* **132**, 036501 (2024).
- [63] B. A. Bernevig and F. D. M. Haldane, Model fractional quantum hall states and jack polynomials, *Phys. Rev. Lett.* **100**, 246802 (2008).
- [64] T. Fukui, Y. Hatsugai, and H. Suzuki, Chern numbers in discretized brillouin zone: Efficient method of computing (spin) hall conductances, *J. Phys. Soc. Jpn.* **74**, 1674 (2005).
- [65] A. Sterdyniak, N. Regnault, and B. A. Bernevig, Extracting excitations from model state entanglement, *Phys. Rev. Lett.* **106**, 100405 (2011).
- [66] A. P. Reddy, F. Alsallom, Y. Zhang, T. Devakul, and L. Fu, Fractional quantum anomalous hall states in twisted bilayer MoTe₂ and WSe₂, *Phys. Rev. B* **108**, 085117 (2023).